Astronomy & Astrophysics

Calibration of NAOS and CONICA static aberrations

Application of the phase diversity technique

A. Blanc[1,2], T. Fusco[1], M. Hartung[3], L. M. Mugnier[1], and G. Rousset[1]

[1] Office National d'Études et de Recherches Aérospatiales, Département d'Optique Théorique et Appliquée,
BP 72, 92322 Châtillon Cedex, France
e-mail: laurent.mugnier@onera.fr

[2] Laboratoire des Signaux et Systèmes, École Supérieure d'Électricité, Plateau de Moulon, 91192 Gif-sur-Yvette, France

[3] Max-Planck-Institut für Astronomie, Königstuhl 17, 69117 Heidelberg, Germany

Abstract. We describe and evaluate the performance of a phase diversity wavefront sensor used to measure the static aberrations of the VLT instrument NAOS–CONICA. The main limitations of this phase diversity technique are compiled. We investigate the systematic errors due to the experimental implementation and the design restrictions. Further error sources stem from the imperfect knowledge of the system, and from limitations of the algorithm. The influence of these errors on the wavefront estimation is evaluated on numerical and experimental data. This study highlights the essential verifications and calibrations needed to obtain accurate results and gives a practical guideline for the application of a phase diversity wavefront sensor. The comprehensive calibration results and the final gain in optical performance are presented and discussed in a complementary paper (Hartung et al. 2003).

Key words. instrumentation: adaptive optics

1. Introduction

The VLT instrument NAOS–CONICA comprised of the adaptive optics (AO) system NAOS[1] (Rousset et al. 1998; Rousset et al. 2000) and the high resolution camera CONICA[2] (Lenzen et al. 1998; Hartung et al. 2000), aims at providing very high quality images on one (UT4-Yepun) of the 8-m telescopes of the Cerro Paranal observatory. To achieve its specification, NAOS has been designed to provide high Strehl ratios ($\geq 70\%$) under good observing conditions. But even if the AO system ideally corrects for atmospheric turbulence, the optical train of CONICA as well as a part of the optical train of NAOS which is not sensed by the wavefront sensor also contribute to the overall degradation of the instrument performance. Indeed, the optical train is not free of aberrations and consequently reduces the Strehl Ratio (SR) on the images. In order to reach the ultimate performance with the instrument, it is necessary to pre-compensate these down-stream static aberrations by the AO system. This is a feature provided by NAOS which is able to introduce known static aberrations on the deformable mirror (DM) in closed loop.

In the NAOS-CONICA instrument it is not possible to introduce an additional wavefront sensor in the optical train of the imaging device CONICA to estimate the wavefront. Hence, the CONICA images themselves must be used to derive the unknown aberrations.

In this paper, we present a phase diversity (PD) (Gonsalves 1982) approach to calibrate these unseen aberrations using a couple of focused and defocused images obtained on the CONICA detector. Because of the huge number of observation modes of NAOS-CONICA, the calibration of the unseen aberrations must be split in several parts: NAOS dichroics, i.e. the beam splitters between the wavefront sensor and imaging paths, and CONICA aberrations, i.e. the different filters and objectives. Detailed explanations of the global calibration procedures as well as a comprehensive presentation of the results are presented in (Hartung et al. 2003) (hereafter called Paper II).

In the present paper we focus on the validation of the phase diversity approach used to estimate these aberrations. In Sect. 2, a description of the phase diversity concept is given along with the specific algorithm used. In Sect. 3, a brief presentation of the experimental setup is proposed. A more

---

[1] NAOS stands for Nasmyth Adaptive Optics System
[2] CONICA stands for COudé Near Infrared CAmera

complete description can be found in Paper II. In Sect. 4, a validation of our PD algorithm is proposed on simulated data. It allows us to assess qualitatively and quantitatively the accuracy of the aberration estimation.

Finally, we exploit the simulations and the experimental results to present the limitations and the overall performance of the aberration calibration procedure in Sect. 5. We list, analyze and quantify all the possible error sources which may induce a loss of accuracy in the PD results. This section allows us to define the optimal parameters to calibrate the whole system.

In Sect. 6, we present a practical example and give a detailed description of the global procedure to estimate NAOS-CONICA static aberrations. This procedure is quite general but the particularities of CONICA and NAOS-dichroic aberration measurements are underlined.

2. Estimation of static aberrations by phase diversity

2.1. Phase diversity principle

The estimation of the aberrations from the sole focused image does not ensure the uniqueness of the solution. This indetermination is due to the relationship between the point spread function (PSF) h and the aberrated phase: a couple (ϕ, ϕ') exists such that $h(\phi) = h(\phi')$. Phase diversity (Gonsalves 1982; Paxman et al. 1992) was proposed to add information and removes this indetermination. The idea is to collect at least one additional image, which differs from the focused one by a known phase variation. Figure 1 illustrates the phase diversity principle. One can note that there are several ways to introduce the known aberration. A possibly non comprehensive list of the possibilities is the following:

- simultaneously using a beam splitter and two detectors as presented in Fig. 1;
- introducing a beam-splitter and a prism and recording the focused and defocused images on the same detector (Gates et al. 1994);
- sequentially using a translation of the detector or introducing the known aberration in the optical path (see Sect. 2.3.2). In this case, it is assumed that the aberrations and the object do not evolve between the two acquisitions (which is the case of the NAOS-CONICA static aberrations for instance).

This technique has been successfully used by some authors to determine aberrations (Carreras et al. 1994; Kendrick et al. 1994; Lee et al. 1997; Thelen et al. 1999; Löfdahl et al. 2000) and also to restore images, as in solar imaging through turbulence (Restaino 1992; Löfdahl & Scharmer 1994; Seldin & Paxman 1994). It uses a low-cost, optically simple wavefront sensor which consists in the imaging camera itself, but it requires a complex numerical and iterative processing to restore the unknowns from the images.
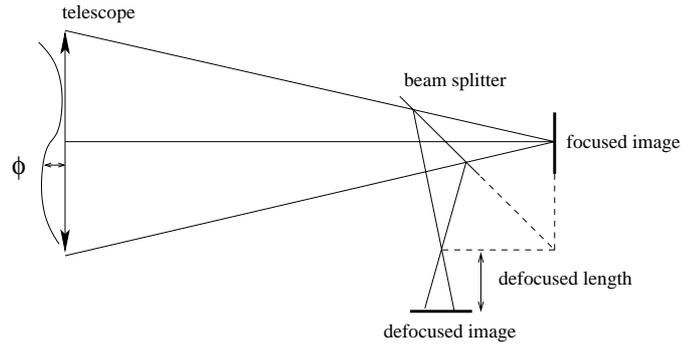

Fig. 1. Phase diversity principle.

2.2. Imaging model

In the isoplanatic patch of the imaging system, the image is the noisy convolution of the PSF h in the observation plane and the object o:

$$i(\boldsymbol{r}) = (h * o)(\boldsymbol{r}) + n(\boldsymbol{r}) \tag{1}$$

where $*$ denotes the convolution product, $\boldsymbol{r}$ is a two-dimensional vector in the image plane and n is an additive noise. The PSF associated with the focused image is given by:

$$h_1(\boldsymbol{r}) = |FT^{-1}\{P(\boldsymbol{u}).\exp[i\phi(\boldsymbol{u})]\}|^2 \tag{2}$$

where $\boldsymbol{u}$ is a two-dimensional vector in the pupil plane, ϕ is the unknown aberrated phase function, P is the aperture function and FT^{-1} denotes the inverse Fourier transform. The phase function is expanded on a set of Zernike polynomials. Indeed, aberrations in an optical system can be mathematically represented by Zernike polynomials (Noll 1976).

$$\phi(\boldsymbol{u}) = \sum_{i=2}^{k} a_i Z_i(\boldsymbol{u}). \tag{3}$$

Theoretically, k should tend to infinity to describe any wave form, but in the particular case of static aberration estimation, the first polynomials (typically the first twenty) are enough to describe the aberrations arising from misalignment of systems made mostly of spherical surfaces or of surfaces with a modest degree of asphericity. In the following, we will note $\boldsymbol{a} = (a_1, ..., a_k)^T$ the unknown aberration coefficients, where T denotes transposition.

In the defocused plane, the PSF is given by:

$$h_2(\boldsymbol{r}) = |FT^{-1}(P(\boldsymbol{u}).\exp\{i[\phi(\boldsymbol{u}) + \phi_{\mathrm{d}}(\boldsymbol{u})]\})|^2 \tag{4}$$

where ϕ_{d} is the known diversity phase function. In our case, $\phi_{\mathrm{d}}(\boldsymbol{u}) = a_4^d Z_4(\boldsymbol{u})$ where Z_4 is the defocus Zernike polynomial. In practice, data are discrete arrays because of the spatial sampling of the images. Equation (1) takes the form:

$$\boldsymbol{i} = \mathrm{H}\boldsymbol{o} + \boldsymbol{n} \tag{5}$$

where H is the Toeplitz matrix corresponding to the convolution by h (Ekstrom & Rhoads 1974), and where $\boldsymbol{i}$, $\boldsymbol{o}$ and $\boldsymbol{n}$ are the discrete forms of the previous variables.

The problem is to estimate the aberration parameters $\boldsymbol{a}$ (the set of a_i) from the data (focused $\boldsymbol{i}_1$ and defocused $\boldsymbol{i}_2$ images) and the defocused distance, without knowing the object $\boldsymbol{o}$.

2.3. Aberration estimation principle

Using a Joint Maximum A Posteriori (JMAP) approach (Little & Rubin 1983), an estimator can be defined as

$$
\begin{aligned}
(\hat{o}, \hat{a})_{\text{JMAP}} &= \arg\max_{o,a} p(i_1, i_2, o, a) \\
&= \arg\max_{o,a} p(i_1|o, a) p(i_2|o, a) p(o) p(a)
\end{aligned} \tag{6}
$$

where $p(i_1, i_2, o, a)$ is the joint probability density function of the data (i_1, i_2), of the object o and of the aberrations a. $p(i_1|o, a)$ and $p(i_2|o, a)$ denote the likelihood of the data i_1 and i_2, $p(o)$ and $p(a)$ are the a priori probability density function of o and a. The noise is modeled as a stationary white Gaussian noise with a variance σ^2 (the same for the two images). In our case, we do not use an explicit probability density function for a ($p(a) = 1$) since the regularization is brought by the small number of estimated Zernike coefficients. Consequently, this joint estimation will be called a Generalized Maximum Likelihood (GML) approach. We choose a Gaussian prior probability distribution for the object with a covariance matrix R_o. The maximization of the a posteriori probability law defined in Eq. (6) is equivalent to the minimization of its neg-logarithm (J_{GML}) defined as

$$
J_{\text{GML}}(o, a) = \frac{1}{2\sigma^2}\|i_1 - H_1 o\|^2 + \frac{1}{2\sigma^2}\|i_2 - H_2 o\|^2 + \frac{1}{2} o^t R_o^{-1} o. \tag{7}
$$

It is important to note that the derivative of $J_{\text{GML}}(o, a)$ with respect to the object gives a closed-form expression for the object $\hat{o}(a)$ that minimizes the criterion for a given a (Paxman et al. 1992). This expression is that of a bi-frame Wiener filter:

$$
\hat{o}(a) = \left(H_1^t H_1 + H_2^t H_2 + \sigma^2 R_o^{-1}\right)^{-1} \left(H_1^t i_1 + H_2^t i_2\right). \tag{8}
$$

Substituting $\hat{o}(a)$ into the criterion yields a new criterion that does not depend explicitly on the object:

$$
J'_{\text{GML}}(a) = J_{\text{GML}}(\hat{o}(a), a). \tag{9}
$$

The interest of this new criterion is its drastic reduction of the solution space.

Furthermore, using a periodic approximation (which corresponds to approximate a Toeplitz by a circulant matrix) (Demoment 1989), the criterion can be expressed in the discrete Fourier domain:

$$
\begin{aligned}
J_{\text{GML}}(o, a) &\propto \sum_f \left[\frac{|\tilde{h}_1(f)\,\tilde{o}(f) - \tilde{\imath}_1(f)|^2}{\sigma^2} \right. \\
&\left. + \frac{|\tilde{h}_2(f)\,\tilde{o}(f) - \tilde{\imath}_2(f)|^2}{\sigma^2} + \frac{|\tilde{o}(f)|^2}{S_o(f)} \right]
\end{aligned} \tag{10}
$$

where $\tilde{}$ stands for a Discrete Fourier Transform (DFT), f the spatial frequency and S_o the power spectral density (PSD) of the object.

Using the same periodicity approximation, $\hat{o}(a)$ can be written as:

$$
\tilde{o}(a) = \frac{\tilde{h}_1^*(f)\,\tilde{\imath}_1(f) + \tilde{h}_2^*(f)\,\tilde{\imath}_2(f)}{|\tilde{h}_1(f)|^2 + |\tilde{h}_2(f)|^2 + \sigma^2/S_o(f)}. \tag{11}
$$

$\tilde{o}(a)$ can be introduced in Eq. (10) so that the new criterion $J'_{\text{GML}}(a)$ only depends on the unknown phase aberrations (a) and can be minimized using an iterative algorithm (for instance a conjugate gradient).

2.3.1. Object regularization

The a priori information required on the object consists in the choice of the object power spectral density model. In our case a focused and a defocused image are acquired with high Signal to Noise Ratio (SNR) and the object is close to be a Dirac function. Consequently the phase estimation can be obtained without any knowledge or estimation of the prior object spectral density. The dimensionless ratio $\sigma^2/S_o(f)$ is simply set to a small arbitrary constant (10^{-6} in our case) in order to avoid numerical problems due to computer precision. Notice that, in the case of lower SNR, the use of a marginal estimator which estimates the sole aberration parameters, gives better results than this ad hoc regularization (Blanc et al. 2000).

2.3.2. Choice of the defocus distance

The choice of the known defocus distance is essential to obtain accurate results. The RMS defocus coefficient a_4^d depends on the defocus distance d of the second image, the telescope diameter D and the focal length F through:

$$
a_4^d = \frac{\pi d}{8\sqrt{3}\lambda(F/D)^2} \text{(in radian)}. \tag{12}
$$

The corresponding peak-to-valley optical path Δ is equal to

$$
\Delta = \frac{\sqrt{3}\lambda a_4^d}{\pi} = \frac{d}{8(F/D)^2}. \tag{13}
$$

In the following sections, a_4^d will be given in nanometers. For NAOS-CONICA, $F/D = 15$. It has been shown (Lee et al. 1999; Meynadier et al. 1999) that a defocus Δ equal to λ provides accurate results. That is a defocus distance equal to 4 mm for $\lambda = 2.2\,\mu\text{m}$. In fact the "optimal" defocus distance depends on the object structure, the phase amplitude ϕ and the SNR on the images. In practice a large domain around this value (typically $\lambda \pm \lambda/2$) still provides accurate results (Meynadier et al. 1999).

In the case of NAOS-CONICA static aberration estimation, two different procedures are applied to introduce the defocus. They are explained briefly in Sect. 3 and in detail in Paper II.

3. Practical implementation

3.1. CONICA calibration

The estimation of CONICA stand-alone aberrations (objectives and filters) is obtained through the use of pinholes (diameter 10 μm) located at different defocused positions in the camera entrance focal plane (0, 1, 2 and 4 mm). The telescope pupil is simulated by a cold pupil placed inside CONICA. A detailed explanation of the experimental setup is given in Paper II. The defocus distances induced through the use of different pinhole pairs are summarized in Table 1.

Table 1. Defocus distances induced by the use of various pinhole pairs. 0–2 and 0–4 pairs are recommended for $J - H$ and K filters respectively.

pinhole pairs	0–1	0–2	0–4	1–4	2–4
Defocus distance (mm)	1.0	2.0	4.0	3.0	2.0

The necessity of introducing enough diversity between the two images and the higher *SNR* of images obtained with the pinhole 0 (which is in the focal plan) lead us to choose the pair 0–2 for *J* and *H* filters and the pair 0–4 for *K* filters. Note that the use of pinholes in the entrance focal plane is not optimal for the phase diversity algorithm since

- the known aberration is not a pure defocus (a longitudinal translation in the entrance focal plane of the camera is not completely equivalent to a detector translation in the imaging focal plane) – see Sect. 5.1.5,
- the use of different pinholes may induce errors in the aberration estimation (the PD algorithm assumes that the same object is used to obtain focused and defocused images, see Sect. 5.1.4). Shape differences between two pinholes can induce phase estimation errors,
- the focused and defocused images are not at the same position on the detector and need to be re-centered – see Sect. 6.2 – since PD can not estimate relative tip-tilt greater than λ between the two images. Indeed, the phase is estimated modulo 2π (see Eqs. (2) and (4)),
- lastly, there may be field aberrations due to the different pinhole position in the beam – see Sect. 5.1.6.

The procedure described in Sect. 2.3 allows us to estimate a set of aberrations for each CONICA configuration, that is a filter plus a camera objective.

3.2. Dichroic calibration

The estimation of the NAOS dichroic aberrations is obtained through the use of the AO system. A focused image of a fiber source, located in the entrance focal plane of NAOS, is recorded in closed-loop in order to avoid the common-path aberrations from the optical train between the source and the dichroic. Then a given defocus is introduced on the DM with the AO loop still closed to record the defocused image. (See Paper II for a complete description of this procedure.) This approach gives the input data for the estimation of the NAOS dichroic aberrations together with the CONICA aberrations. The value of the separated dichroic aberrations is obtained by subtracting the value of the previously estimated CONICA aberrations.

The introduction of a defocus by the DM avoids the difficulties of object defocussing highlighted above for the CONICA calibration. Now, the same object is considered and thus the two images are located at the same position on the detector.

4. Simulation results

In order to validate the algorithm and to quantify its precision, we first consider simulated images. The conditions for this
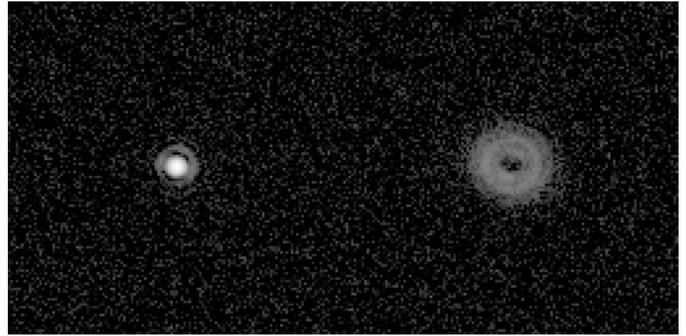

Fig. 2. Simulated focused and defocused images (logarithmic scale). Noise is added to obtain a *SNR* of 200 in the focused image.

simulation are given by a point-like object, an imaging wavelength of 2.166 μm and a pure defocus equal to λ (peak to valley) between the two images, corresponding to a defocus coefficient a_4^d of 641.5 nm RMS. We degrade the PSF by a wavefront deformation described by its Zernike coefficients. The coefficients are arbitrary but chosen to have comparable values as observed in the calibration procedure (see Paper II). The phase is generated with the first 15 Zernike polynomials, note that the estimated phase will be expanded on the same polynomials. We add white noise to each image in order to obtain a *SNR* of 200 which corresponds roughly to the *SNR* of the CONICA data (this is the typical average *SNR* corresponding to the time exposure used, which has been estimated on several measurements). The *SNR* is defined as the ratio of the maximum flux in the focus image over the RMS noise. The same noise statistics is applied to the defocused image. That results in a lower *SNR* on this image since the defocus spreads the PSF and reduces its maximum value. The focused and defocused images are presented in Fig. 2. In this example only two possible limiting parameters (see Sect. 5) have been taken into account: noise and image re-centering. The system is assumed to be perfectly adjusted and the images to be perfectly pre-processed without having any residual background features.

Figure 3 shows a comparison between the input images of the simulation and the PSFs being reconstructed by the estimated aberrations and visualizes the quality of the aberration estimation. This visualization is helpful to judge real calibration data when only in-focus and out-of-focus images are available. Table 2 quantifies the performance of wavefront estimation by comparing the true and the estimated Zernike coefficients. On each coefficient a good accuracy is obtained: the errors are less than a few nanometers. The maximum error is for the two astigmatisms. The influence of *SNR* on estimation results is analyzed in Sect. 5.

The slight tip-tilt introduced between the two input images ($a_2 = 70$ nm rms and $a_3 = -103$ nm RMS) are estimated with a high precision, too. The error amounts to less than 1% (the tip-tilt values are not shown in Table 2). In the next section, we focus on the possible sources for losses of estimation accuracy.
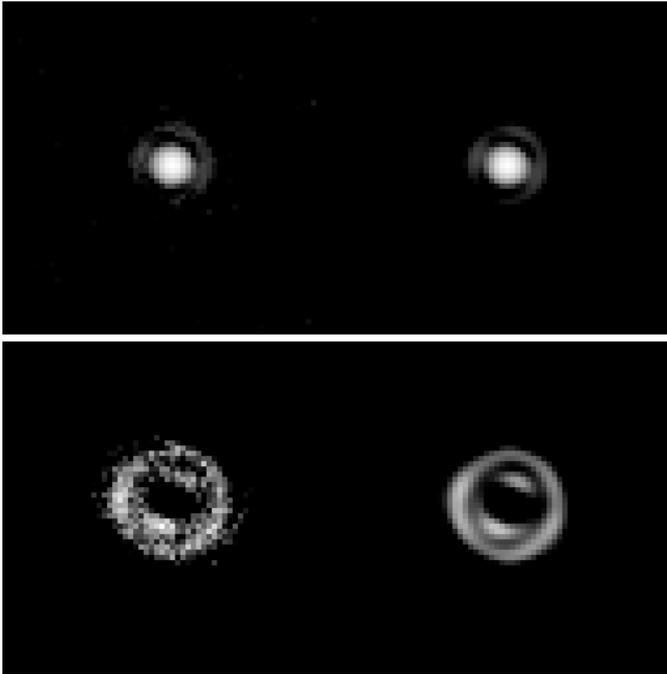
Fig. 4. Influence of the error on defocus distance on estimated aberration by phase diversity. The CONICA camera C50S and the narrow band filter Br_γ are used. The focused and defocused images are obtained using the 0–4 pinhole pair (that is a theoretical defocus of 4 mm between the two images). For the same couple of images several defocus distances (from 3.8 to 4.2 mm) serve as input parameters.

Fig. 3. Comparison between images (left) and reconstructed PSFs (right) from estimated aberrations. On top the focused images, at the bottom the defocused images (logarithmic scale and zoom×2 are considered for each image).

Table 2. Comparison between true and estimated Zernike coefficients applying phase diversity to simulated data with an image *SNR* equal to 200. The absolute value of the error is given for each coefficient. The total error is equal to 9.3 nm RMS.

Zernike number	true (nm)	estimated (nm)	error (nm)
4	60.5	61.5	1
5	−39.3	−46.7	7.4
6	58.1	61.7	3.6
7	−16.2	−15.9	0.3
8	−14.1	-10.9	3.1
9	−2.5	−3.6	1.1
10	13.7	12.9	0.7
11	−24.3	−26.	1.7
12	0.5	1.2	0.7
13	−3.2	−4.9	1.7
14	2.8	3.3	0.4
15	−2.4	−2.2	0.2

5. Limitations

The PD algorithm is based on several assumptions which must be well verified to obtain a good accuracy on the results. A list of possible error sources is given below. Quantitative results are essentially given on experimental data and with additional simulation data when necessary. The global procedure of data reduction can be found in Sect. 6. The error sources can be decomposed in three parts: the errors due to a non-perfect knowledge of the system (calibration errors or uncertainties), the errors d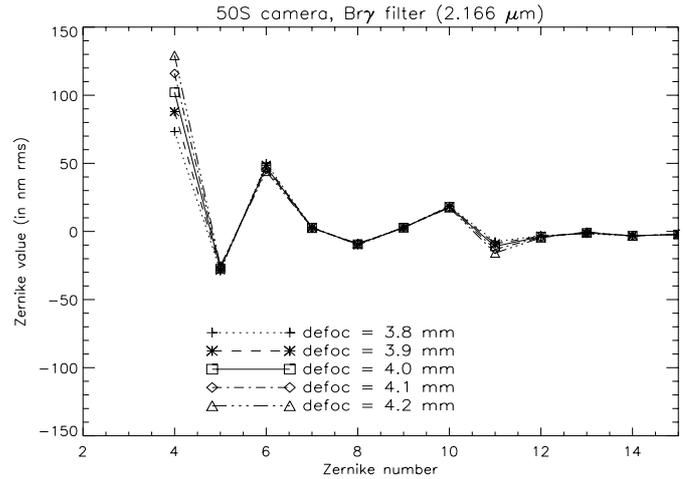ue to the image acquisition and pre-processing (noise, residual background, etc.) and the errors due to limitation of the algorithm (spectral bandwidth, amplitude of the estimated aberrations, etc.).

5.1. System limitations

Let us first focus on the errors due to the imperfect system knowledge.

5.1.1. Defocus distance

The major assumption of the PD principle is the addition of a *known* distortion (defocus in our case) between two images. An error on the defocus induces an error on the coefficients of radially symmetric aberrations, with a main part on the estimated defocus itself (see Fig. 4). The difference between the maximal and the minimal estimated value of the defocus coefficient is 55 nm. For the spherical aberration, it is 10 nm and for the other ones, it is less than 5 nm.

In addition one can show in Fig. 5 that for reasonable errors on the known defocus, the propagation error coefficient is equal to one. Hence, the uncertainty on the known defocus distance yields directly the uncertainty on the estimated defocus aberration.

This uncertainty on the defocus distance can be due to:

– an uncertainty on the physical position of the CONICA pinholes in the entrance focal plane. This uncertainty is estimated to ±0.15 mm corresponding to $\Delta a_4 = \pm 24$ nm RMS;
– a systematic uncertainty on the F/D ratio (estimated to be less than two percent);
– the precision of a focus adjustment with the NAOS deformable mirror for the dichroic aberration estimation. This error is estimated to less than a few percent.
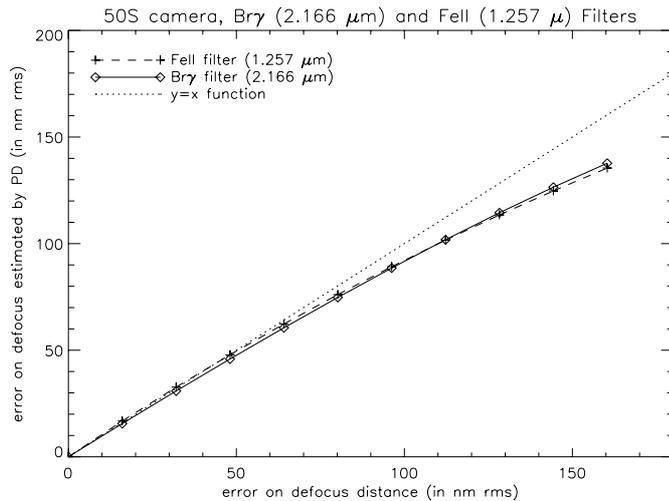
Fig. 5. Influence of the error on defocus distance on the estimation of the defocus. Experimental data have been used. The results are given for the CONICA camera C50S and two narrow band filters: FeII (1.527 μm) and Br$_\gamma$ (2.166 μm). The pinhole pair 0–2 (that is a theoretically defocus of 2 mm) and 0–4 (that is a theoretically defocus of 4 mm) are respectively used for FeII and Br$_\gamma$ filters. For each couple of images several defocus distances (respectively from 1.5 to 2.5 mm and from 3.5 to 4.5 mm for FeII and Br$_\gamma$ filters) serve as input parameters.

All these items lead to a precision of the estimated defocus roughly equal to a ± 30 nm. It will be shown in the following that the error on the defocus distance is by far the dominant error for our application.

5.1.2. Camera pixel scale

The camera pixel scale is needed to calculate the oversampling factor. An error on this factor induces an error on the coefficients of all radially symmetric aberrations (defocus, spherical aberration ...) as shown in Fig. 6.

An error of the pixel scale is essentially propagated to the defocus aberration estimation. The difference between the maximal and the minimal estimated value of the defocus coefficient is 17 nm. A slight error of 6 nm can be seen on spherical aberration but remains negligible in comparison to the one on the defocus. In Fig. 7 the evolution of the estimation error of the defocus coefficient is plotted as a function of a pixel scale measurement error. It is assumed that the true value is 13.25 mas measured during the firs on-sky tests of the AO system. Since the accuracy on the pixel scale measurement is better than 0.2 mas, one can estimate the wavefront error (WFE) due to this uncertainty to be less than a few nanometers and therefore to remain negligible.

5.1.3. Pupil shape

An exact knowledge of the pupil shape (diameter, central obstruction, global shape) is required. In particular, few percent of mis-alignment of the pupil leads to an error of a few tens nanometers on the phase estimation.
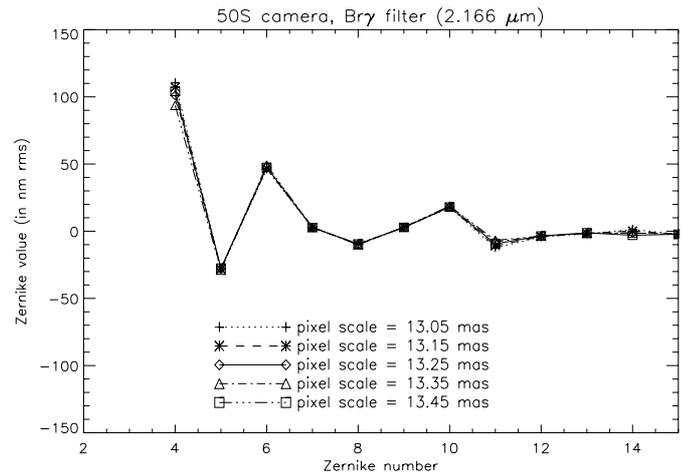

Fig. 6. Influence of the pixel scale error on estimated aberration by phase diversity. Experimental data have been used. The CONICA camera C50S and the narrow band filter Br$_\gamma$ are used. The focused and defocused images are obtained using the 0–4 pinhole pair. For the same couple of images several pixel scales (from 13.05 to 13.45 mas) serve as input parameter for the PD algorithm.
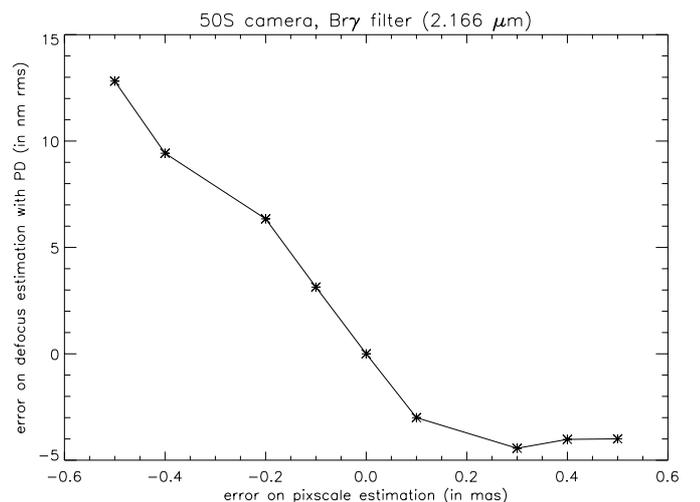

Fig. 7. Influence of the pixel scale error. The reference value is set to 13.25 mas. For this value it is *assumed* that the error on the defocus coefficient estimation is zero (the experimental conditions are the same as in Fig. 6).

5.1.4. Differential object structures

The algorithm is based on the assumption that the same object is used to obtain the focused and the defocused image. If two different objects are used (case of CONICA pinholes), errors could be induced if they are not completely identical. Figure 8 shows for the narrow band filter FeII (1.64 μm) and the objective C50S the estimated aberration for different pinhole pairs. It shows a good agreement between all the pinholes, except for the pinhole pair 0–1. The discrepancy in the estimated aberrations can probably be attributed to the small defocus distance. Disregarding the pair 0–1, the good agreement of all the other pairs leads us to assume the pinholes close to be identical. Indeed, the main part of the WFE is due to the defocus
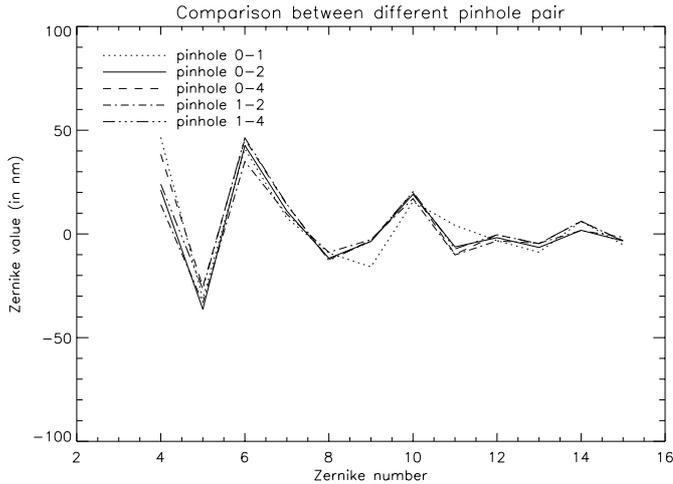
Fig. 8. Comparison of the estimated aberrations of various pinhole pairs. Camera C50S with FeII narrow band filter (1.644 μm).

Fig. 9. Evolution of the wavefront error as function of *SNR* on focal plane image. Simulation presented in Sect. 4 have been used. A 1/*SNR* theoretical behavior is plotted for comparison.

coefficient and highlights the uncertainties on pinhole positions as already mentioned in Sect. 5.1.1.

5.1.5. Translation in the entrance focal plane

The maximal detector translation along the optical axis is not enough to introduce significant diversity between focused and defocused images. For the calibration of CONICA aberrations, we introduce defocus by translating "the object" in the entrance focal plan. As we said before (Sect. 3.1), this implementation does not create exactly a pure defocus but also in first order, some spherical aberration. We have quantified the deviation from a pure defocus by using the optical design software ZEMAX and shown that it can be neglected (a translation of 4 mm in the entrance focal plan induces defocus and a negligible spherical aberration $a_{11} = 0.14$ nm).

5.1.6. Field aberrations

The images obtained by the pinhole 1 and 2 are not located at the same position on the detector than those obtained by the pinhole 0 and 4 (separation of 100 pixels in y). It induces that some focused and defocused images (for example pair 0–1 and 0–2) do not see exactly the same aberrations. The evolution of the field aberrations has been evaluated by optical calculations using ZEMAX. This study has shown that the main influence concerns the astigmatism a_5 but in a negligible way (its variation is less than 5 nm for a separation of 100 pixels in x and 100 pixels in y).

5.2. Image limitations

5.2.1. Signal to noise ratio

The accuracy of the PD algorithm is directly linked to the signal to noise ratio in the images (the definition of *SNR* is given in Sect. 4). We present in Fig. 9 the WFE error evolution as a function of image focal plane *SNR* This figure, obtained on simulated data, shows the perfect agreement
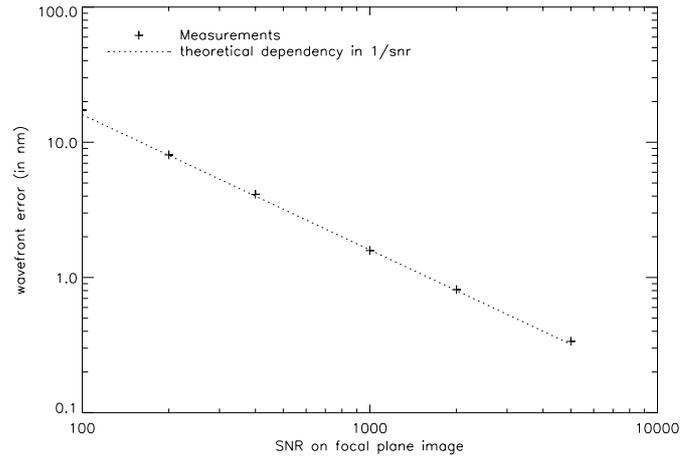
between simulation and expected (theoritical) 1/*SNR* behavior (Meynadier et al. 1999). For the NAOS-CONICA aberration estimation it has been checked that the *SNR* is high enough to make this error source negligible in comparison to the others since the typical values of *SNR* are greater than a few hundred. That leads to a WFE of a few nanometers due to signal to noise ratio. This has been experimentally checked on one set of data. Four pairs of focused-defocused images have been recorded sequentially in the same CONICA configuration (FeII filter and camera C50S). The *SNR* on these images is 400. Aberrations are then estimated for each couple and the WFE fluctuation on this four set of coefficients is equal to 2.2 nm RMS, which is in perfect agreement with Fig. 9 (obtained on simulation).

5.2.2. Residual background features

The principle of the PD method is the minimization of a criterion (Eq. (10)) which is based on a convolution image model (Eq. (1)). Thus the image should be perfectly corrected for all instrumental features (background, dead pixels, etc.) in order to match the model. In practice, residual features are still present. In particular, in the case of CONICA images, a background fluctuation due to pick-up noise can induce residual features on the images even after a proper background calibration (see Sect. 6.2). These features are interpreted as signal by the phase-diversity algorithm. Therefore they induce bias on the aberration estimation. The effect of such fluctuations is highlighted in Fig. 10 on experimental data. The difference of the PD results obtained with and without residual background features yield the WFE which is plotted as a function of the image size. This can be understood as a function of the residual background influence, too, because it obviously depends on the image size: the smaller the images, the less important the residual background in comparison to the signal. Nevertheless, the image size should be large enough to contain the whole signal. Furthermore, the modelisation of the pupil shape (see Sect. 5.3.3) must also be taken into account to choose the right
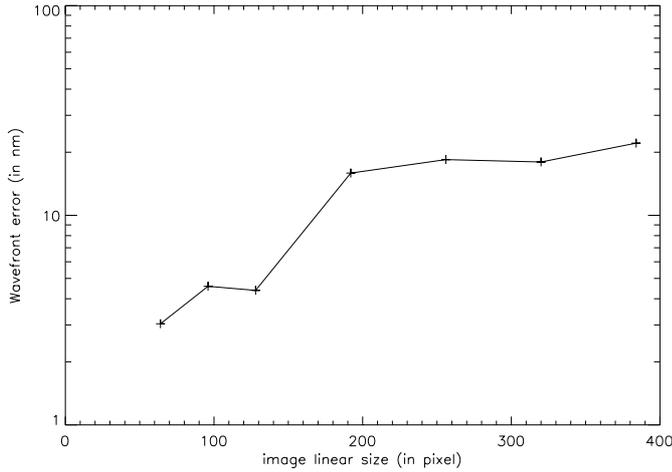
Fig. 10. Evolution of the wavefront error as a function of the image size. Experimental data have been used.
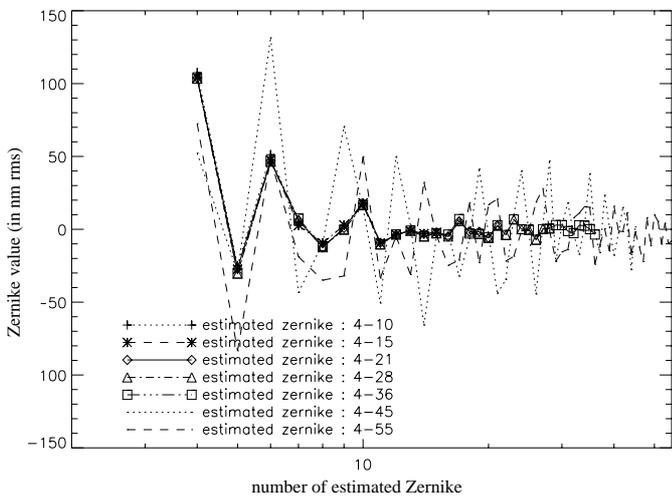

Fig. 11. Evolution of the aberration estimation as a function of the number of Zernike in PD algorithm. Experimental data have been used.

image size. In Sect. 6.2 we describe a pre-processing algorithm which allows to remove these residual background features.

5.2.3. Number of estimated Zernike polynomials

As presented in Sect. 2.3, the phase regularization in our algorithm is provided by a truncation of the solution space through the use of a finite (and small) number of unknowns (typically the first twenty Zernike coefficients). Figure 11 shows, on experimental data, the influence of the number of estimated Zernike on the reconstruction quality. Note that, in the case of measurements of CONICA stand-alone aberrations, the pupil is unobscured and thus the Zernike polynomials are strictly orthogonal.

There exists a limit to the number of Zernike polynomials that can be estimated with a reasonable accuracy. Of course this limit depends on the signal to noise ratio on the images. In the present case, this number is equal to 36. Note that if a more sophisticated regularization term is introduced in the
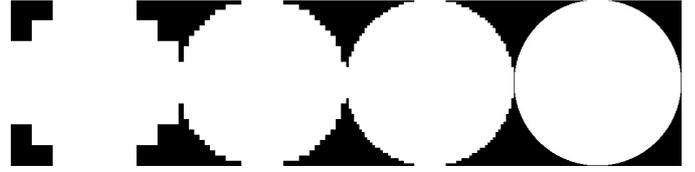

Fig. 12. Pupil shape in the PD algorithm for three numbers of pixel used in the pupil sampling [8, 32, 64 and 256]. The oversampling factor of 2 in K band leads to corresponding image sizes equal to [32, 128, 256 and 1024].

PD algorithm both on the object and the aberrations this limitation should be overcome. Nevertheless such a regularization is not needed here since the aberration amplitudes are negligible (less than a few nanometers) for Z_i above $i = 11$ (i.e. the spherical aberration). The WFE between estimated Zernike coefficients 4–15 and estimated Zernike coefficients 4–36 is about 1.3 nm RMS. This WFE is very small and thus shows that the aliasing of the Zernike polynomials above 15 on the estimated coefficients 4–15 is negligible.

5.3. Algorithm limitations

5.3.1. Spectral bandwidth

The phase diversity concept proposed here is a monochromatic wave-front sensor (theoretically the concept can be applied on polychromatic images but it induces an important modification of the algorithm to model the data (Seldin & Paxman 2000)). Nevertheless it has been shown (Meynadier et al. 1999) that the use of broadband filters does not significantly degrade the accuracy as long as $\frac{\Delta\lambda}{\lambda}$ is lower than a few tens of percents (typically $\frac{\Delta\lambda}{\lambda} \leq 0.15$).

5.3.2. Image centering

As mentioned above, the PD algorithm can not estimate a tip-tilt between the two images larger than 2π. Therefore, a fine centering between focused and defocused images must be done before the aberration estimation (see Sect. 6.2).

5.3.3. Pupil model

Since we consider here experimental data (see Sect. 6), the modelisation of the pupil shape in the algorithm is critical, in particular the pixelisation effects. Indeed, in PD algorithm the pupil definition depends on the image size and on the oversampling factor. For example, images of camera C50S in K band oversample with a factor of 2 and a 32×32 image will lead to a pupil diameter of 8 pixels (see Fig. 12). In this case, the pixelisation effects on the shape of the pupil will induce aberration estimation error. These effects are illustrated in Fig. 13.

Therefore, large images are recommended to well model the pupil and to obtain accurate results. Nevertheless, two problems may occur with the processing of large images:

– a residual background problem (see Sect. 5.2.2). The larger the image, the more important the effects of residual
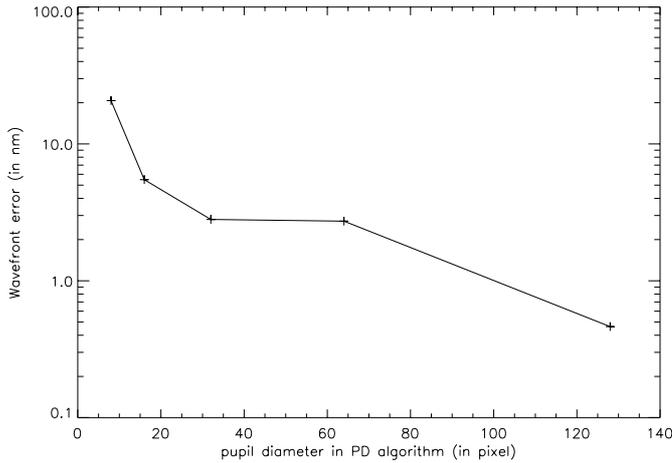
Fig. 13. Evolution of the wavefront reconstruction error as function of pupil sampling in PD algorithm. The x axis gives the pupil diameter in pixel in the PD algorithm.

background unless the images are tapered outside their central region;

– a computation time problem. Because of the iterative resolution of criterion defined in Eq. (7), the increase of images size will lead to an increase of computation time.

This highlights the choice of a good compromise between pupil model in the PD algorithm to avoid phase reconstruction error and a reasonable image size.

The evolution of the reconstruction error as a function of pupil sampling is presented in Fig. 13. To minimize the residual background effects, all the background pixels (that is pixels with no PSF signal) has been put to zero in the images.

Considering the results shown in Figs. 13 and 10 along with the computation load lead us to choose an image size equal to 128×128 pixels for the K band and 64×64 pixel for the J band.

5.4. Conclusion

In this part, we have analyzed and quantified, on experimental and simulated data, the possible sources of errors in the static aberration estimation for NAOS-CONICA. It is shown that the main source of errors is due to an imperfect knowledge of the system (that is calibration errors). In particular a precise knowledge of the defocus distance between focused and defocused planes is essential.

If very high precisions are required on the estimation and on the correction of static aberrations (for instance in the case of a future very high SR AO for exo-planet detection), the PD must be taken into account in the early design of the system in order to optimize with respect to the constraints and error sources listed above.

6. Practical example

In this section we give a detailed description on a practical example of the global procedure used to estimate NAOS-CONICA static aberrations. This procedure is quite general but

the particularities of the CONICA and NAOS dichroic aberration measurements are underlined. All the illustrations are obtained for the following configuration of CONICA: objective C50S (pixel size equal to 13.25 mas) and Br_γ filter.

6.1. Input data

The input data are a focused and a defocused image ($i_{1,2}$) with their associated backgrounds ($b_{1,2}$) and a known defocus distance expressed in mm in the entrance focal plane of CONICA. This distance is given by the pinhole choice in the case of CONICA measurements (see Table 1) or by the defocus introduced by the DM in the case of the NAOS dichroic aberration measurements. In the example we consider the first approach and introduce the defocus by the pinhole choice.

6.2. Pre-processing

The pre-processing of the images is required before the wavefront can be estimated. We split the pre-processing in several steps:

– Conventional background subtraction in order to remove the main part of detector defects (bad pixels, background level, possible background features, etc.):

$$i_{1,2}^{corr} = i_{1,2} - b_{1,2}. \tag{14}$$

The division by a flat-field pattern is recommended to increase the accuracy of the results even if it is not done in this example.
– The focused and defocused images are re-centered by a correlation procedure. For each filter we computed the relative shifts of the PSFs against each other. The median of these shifts was determined and serves to re-center the defocused images. This procedure ensures that re-centering is accurate enough to obtain a relative tip-tilt between the two images lower than 2π.
– Removing of the residual background feature: the most important feature is a residual sine function in vertical direction due to pick-up noise. Its amplitude is greater than the noise level. An estimation of the residual background features is necessary and performed directly on the images using a median filter in horizontal direction applied to each image column. A comparison of the images before and after this residual feature removal is presented in Fig. 14.
– Image windowing: the image size is a trade-off between a good numerical pupil modeling and a reasonable computation time. We achieve reliable results by using 128×128 frames.

Note that we have assumed that all the bad pixels have been removed by the background subtraction. If some of them are still present in the pre-processed images, they must be removed by hand to ensure that they do not induce reconstruction errors in the PD algorithm.
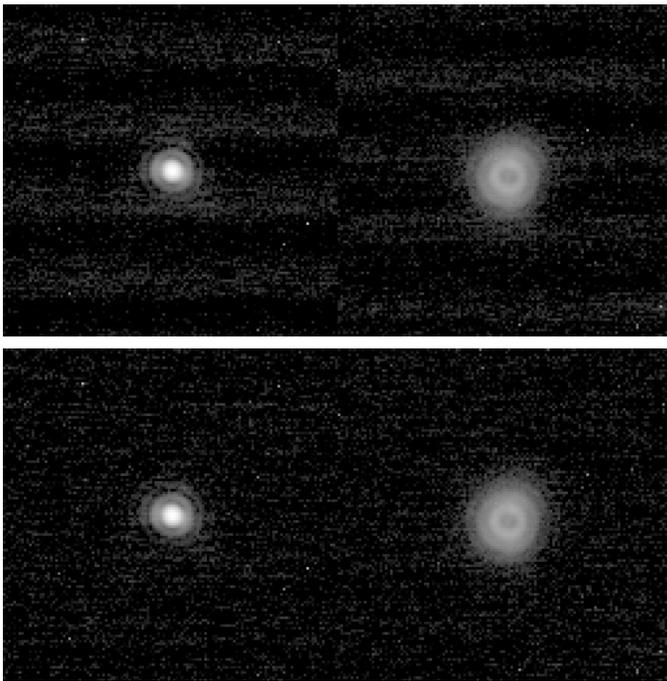
Fig. 14. Comparison of focused and defocused images before (on top) and after (at the bottom) the application of an algorithm which removes residual background features (log scale). The estimated *SNR* is equal to 400.

6.3. CONICA aberration estimation

When both focused and defocused images have been pre-processed as described above, the PD algorithm can be applied. The inputs of the PD algorithm are:

- pixel scale: 13.25 mas (camera C50S);
- central obstruction given by the fraction of the pupil diameter: 0 (full pupil);
- wavelength (in μm): 2.166 (Br$_\gamma$ filter);
- highest estimated Zernike number: 15 (estimation of Zernike polynomials from 4 up to 15);
- defocus coefficient a_4^d (in nm RMS): in the present example, $d = 4$ mm which leads to $a_4^d = -641.5$ nm;
- the focused and defocused images obtained after pre-processing.

The results obtained are summarized in Table 3. A bad background correction leads to an important error on the defocus ($\simeq$20 nm). A comparison between focused and defocused images and reconstructed PSFs from the estimated Zernike is proposed in Fig. 15. The estimated SR on the 12 estimated Zernike is equal to 87%. It compares nicely to the SR directly computed on the focal plane image, which is equal to 85%.

7. Conclusion

We have given a precise description of the phase diversity algorithm developed at ONERA and of its use for the calibration of NAOS-CONICA static aberrations. The concept of phase diversity has first been recalled, then the expression of the

Table 3. Measured aberrations (in nm RMS) for the CONICA camera C50S and the Br$_\gamma$ filter. The defocus distance between the two images is 4 mm and the estimated *SNR* is 400. Only the 12 first Zernike 4-15 are given. The raw values are obtained without residual background subtraction. The corrected ones are obtained after subtraction of the residual background features.

Zernike	4	5	6	7	8	9
aberration (nm)						
raw	91	−27	48	3	−9	−4
aberration (nm)						
corrected	112	−24	47	1	−5	−1

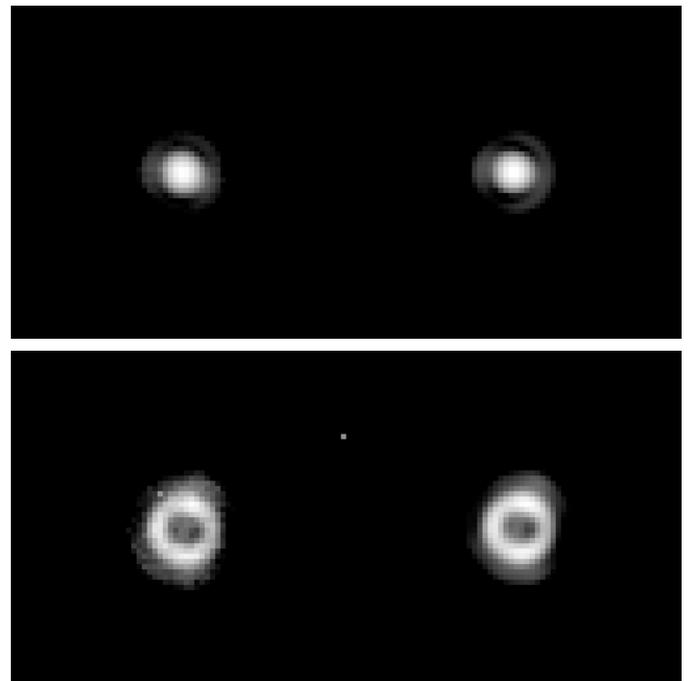| Zernike	10	11	12	13	14	15
aberration (nm)						
raw	19	−20	−5	−1	1	−2
aberration (nm)						
corrected	17	−19	−3	−2	−3	−3

Fig. 15. Comparison between images (left) and reconstructed PSF from estimated aberrations (Right). (up) focused image, (down) defocused image (log scale are considered for each image).

criterion to be minimized has been given. Guidelines for a practical implementation have been proposed. The essential parameters of the algorithm have been studied. This has allowed us to highlight the essential verifications and calibrations needed to obtain accurate results with PD.

First, a simulated example of utilization has been proposed in order to demonstrate the precision of the estimation under typical *SNR* conditions of acquisition of NAOS-CONICA images. It shows that for a *SNR* of 200, the error on the aberration estimation is less than few nanometers per polynomial.

This simulation gives the ultimate performance for a given *SNR* since it does not account for experimental uncertainties and bias.

The limitations of the experimental approach have been listed and studied. It has been shown that the main source of error is induced by the uncertainty on the pinhole distances which leads to an error on the defocus estimated to ±24 nm. An other source of degradation is due to the bad knowledge of the pixel scale which contributes for a few nanometers on the defocus. Furthermore, an exact knowledge of the pupil alignment is required to ensure a good estimation of the aberrations. The residual background after compensation in the images is another important source of degradation, estimated to a few tens nanometers. In the case of the images of NAOS-CONICA, the *SNR* is high enough to make this error source negligible in comparison to the others.

All these error sources lead to an uncertainty on the aberration estimation: ±35 nanometers on the defocus and around few nanometers for the high order Zernike polynomials.

Finally, an example of processing of experimental data obtained on CONICA during commissioning at the VLT has been given. Pre-processing required to minimized the Camera defects has been described and a comparison of focal plane PSFs with reconstructed PSFs using estimated aberrations has been made. It shows good agreements both in term of PSF shape and SR measurements.

It has been shown that Phase Diversity is a simple and powerful approach to compute unseen aberration of an AO system. This is of a great interest for future very high SR system in which an accurate estimation and correction of such aberrations is essential to achieve the ultimate performance and to reach the scientific goals (exo-planet detection for instance).

References

Blanc, A., Idier, J., & Mugnier, L. M. 2000, in UV, Optical, and IR Space Telescopes and Instruments, Proc. Soc. Photo-Opt. Instrum. Eng., ed. J. B. Breckinridge, & P. Jakobsen (Bellingham, Washington), SPIE, 4013, 728

Carreras, R. A., Restaino, S., & Duneman, D. 1994, in Image Reconstruction and restoration, Proc. Soc. Photo-Opt. Instrum. Eng., SPIE, 2302, 323

Demoment, G. 1989, IEEE Trans. Acoust. Speech Signal Process, 37, 2024

Ekstrom, M. P., & Rhoads, R. L. 1974, J. Comput. Phys., 14, 319

Gates, E. L., Restaino, S. R., Carreras, R. A., Dymale, R. C., & Loos, G. C. 1994, in Image Reconstruction and Restoration, Proc. Soc. Photo-Opt. Instrum. Eng., SPIE, 2302, 330

Gonsalves, R. A. 1982, Opt. Eng., 21, 829

Hartung, M., Bizenberger, P., Boehm, A., et al. 2000, in Optical and IR Telescope Instrumentation and Detectors, Proc. Soc. Photo-Opt. Instrum. Eng., ed. M. Iye, & A. F. Moorwood, SPIE, 4008, 830

Hartung, M., Blanc, A., Fusco, T., et al. 2003, A&A, 399, 385

Kendrick, R. L., Acton, D. S., & Duncan, A. L. 1994, Appl. Opt., 33(27), 6533

Lee, D., Welsh, B., & Roggemann, M. 1997, Opt. Lett., 22, 952

Lee, D. J., Roggemann, M. C., & Welsh, B. M. 1999, J. Opt. Soc. Am. A, 16, 1005

Lenzen, R., Hofmann, R., Bizenberger, P., & Tusche, A. 1998, in Infrared Astronomical Instrumentation, Proc. Soc. Photo-Opt. Instrum. Eng., SPIE, 3354, 606

Löfdahl, M. G., & Scharmer, G. B. 1994, A&A, 107, 243

Löfdahl, M. G., Scharmer, G. B., & Wei, W. 2000, Appl. Opt., 39, 94

Little, R. J. A., & Rubin, D. B. 1983, The American Statistician, 37, 218

Meynadier, L., Michau, V., Velluet, M.-T., et al. 1999, Appl. Opt., 38, 4967

Noll, R. J. 1976, J. Opt. Soc. Am., 66(3), 207

Paxman, R. G., Schulz, T. J., & Fienup, J. R. 1992, J. Opt. Soc. Am. A, 9, 1072

Restaino, S. 1992, Appl. Opt., 31, 7442

Rousset, G., Lacombe, F., Puget, P., et al. 2000, in Adaptive Optical Systems Technology, Proc. Soc. Photo-Opt. Instrum. Eng., ed. P. L. Wizinowich (Bellingham, Washington), SPIE, 4007, 72

Rousset, G., Lacombe, F., Puget, P., et al. 1998, in Astronomical Telescopes & Instrumentation, Proc. Soc. Photo-Opt. Instrum. Eng., ed. D. Bonaccini, & R. K. Tyson (Kona, Hawaii), 3353

Seldin, J., & Paxman, R. 2000, in Imaging Technology and Telescopes, SPIE, 4091-07

Seldin, J. H., & Paxman, R. G. 1994, in Image Reconstruction and Restoration, SPIE, 2302

Thelen, B. J., Paxman, R. G., Carrara, D. A., & Seldin, J. H. 1999, J. Opt. Soc. Am. A, 16, 1016